GEOPERSIA

Accepted Manuscript

Geodynamics and tectonic setting of volcanic rocks from Tineh to Reineh (Haraz road) in Iran

Ramin Mazandarani, Seyed Jamal Sheikh Zakariaee, Seyed Mojtaba Mortazavi, Mansur Vosoughi Abedini, Abdollah Yazdi

Accepted Manuscript

Geodynamics and tectonic setting of volcanic rocks from Tineh to Reineh (Haraz road) in Iran

Ramin Mazandarani [1] (iD), **Seyed Jamal Sheikh Zakariaee** [1] , *(iD), **Seyed Mojtaba Mortazavi** [2] (iD), **Mansur Vosoughi Abedini** [3] (iD), **Abdollah Yazdi** [4] , † (iD)

[1] Department of Earth Sciences, SR.C., Islamic Azad University, Tehran, Iran
[2] Department of Mining Engineering, Sava.C., Islamic Azad University, Savadkooh, Iran
[3] Department of Geology, Shahid Beheshti University, Faculty of Earth Sciences, Tehran, Iran
[4] Department of Geology, Kah.C., Islamic Azad University, Kahnooj, Iran

Abstract

Damavand Stratovolcano, with a height of 5610 meters above sea level, is the highest volcano in Iran and the Middle East. Located about 50 km northeast of Tehran, this mountain is currently experiencing fumarole activity. On the Haraz road, the main volcanic rocks of the mountain are olivine basalt, trachyandesite, and basalt trachyandesite. These rocks are primarily composed of minerals such as olivine, clinopyroxene (augite), phlogopite, apatite, iron oxides, amphibole (pargasite), and zircon. The chondrite-normalized and primitive mantle-normalized multi-element spider diagrams of these rocks reveal their enrichment in LILEs and LREEs, along with depletion in HFSEs and HREEs (such as Ti and Nb). These geochemical signatures reflect characteristics of both subduction-related and ocean island basalt (OIB) environments for these rocks, suggesting a deep mantle source for their parent magma. In this respect, the local rise of deep-mantle materials beneath the Alborz Mountains might have led to the eruption of intraplate Damavand lavas. Compressional stress applied to the Iranian plate after the closure of Neotethys - leading to mantle uplift - was a potential cause of subcontinental lithosphere delamination. The eruption of intraplate Damavand lavas appears to be linked to the localized upwelling of deep mantle material beneath the Alborz Mountains. This mantle ascent may have been triggered by compressional forces on the Iranian plate following the closure of the Neotethys Ocean, potentially causing delamination of the sub-continental lithosphere.

Keywords: Damavand Stratovolcano; Geochemistry; Volcanic rocks; Haraz; Iran.

Introduction

Damavand Stratovolcano is situated in the central part of the Alborz Mountains, along the southern margin of the Caspian Sea. The Central Alborz is characterized by an asymmetric "V-shaped" structure that separates faults and folds with a Northwest-Southeast strike to the west from a Northeast-Southwest trend to the east (Berberian, 1976) (Fig. 1a). Since the area is still affected by tectonic motions (Allen et al., 2003; Vernant et al., 2004), no isostatic balance has been established in the Alborz region (Moin Vaziri, 1998). The primary volcanic products of Damavand are trachyandesite-trachyte lavas and pyroclastic materials (e.g., pyroclastic and epiclastic flows) characterized by a low spread on the sedimentary foundation of this volcano. The spread of pyroclastic materials is more widespread in the southern and southeastern parts of the region. The Damavand volcano is located 20 km north of the active Mosha fault. Other known faults in the Damavand region include the Asak, Baijan, Nova, Sefid Ab, Shahandasht,

---

* Corresponding author e-mail: Sheikhzakariaee@srbiau.ac.ir

† Corresponding author e-mail: abdollah.yazdi@iau.ac.ir

and Vararoud faults. According to the gravity modeling by (Dehghani & Makris, 1984), the crust thickness in the Alborz is about 35 km. However, based on seismic data, this thickness ranges from 45 km (Asudeh et al., 2010) to 58.2 km in the southern parts of the Central Alborz (Abbasi et al., 2010). In another study, (Sadudi et al., 2009) estimated the abnormal thickness of the crust at a depth of 67 km below the Damavand volcano.

Salehzadeh et al., (2022) investigated the textural evidence of plagioclase in flows, fallout, and flow ash from Young Damavand. These authors confirmed the existence of distinct magma reservoirs and the movement of magma among these reservoirs at varying depths.
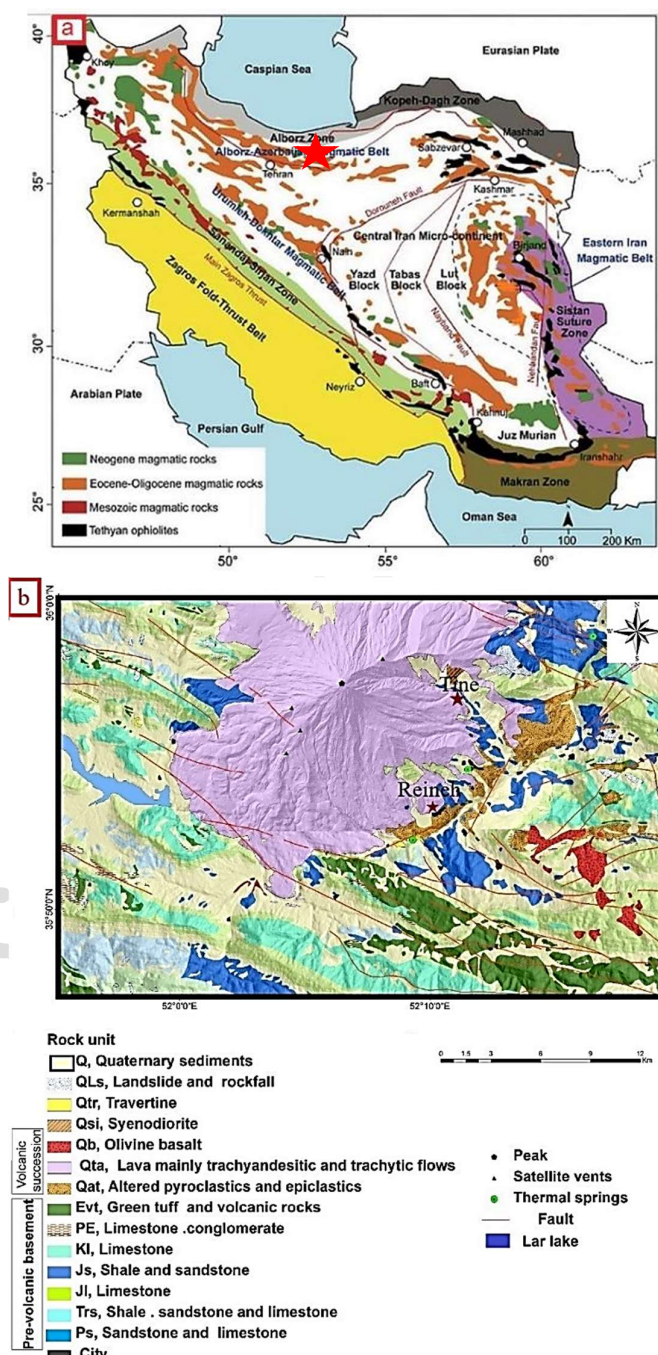

Figure 1. a) The geological map of Iran (Stocklin & Nabavi, 1973) and b) The study area (Eskandari et al., 2018)

Young lava flows, along with conglomerate and alluvial material, have spread to the Dalichai River in the west and to Haraz in the south. Very fine ashes and lahars appear as thick-layered agglomerates covered by very thick flood conglomerates. The main lavas of Damavand are composed of Trachyandesite and Trachyte. These lavas make up the Lar formation and other sediments in the Haraz route. Basaltic tuff and scoria are also seen in the lower part of basaltic lavas. Most of the lavas in the study area show the final phase of the Damavand eruption. However, according to (Allenbach, 1966), the reversal phenomenon in the lava sequence has led to the placement of newer lavas under older lavas in parts of Damavand.

Considering the mentioned points, this paper presents a summary of our field observations and geochemical studies of volcanic rocks in the Haraz Road area, aiming to understand the petrogenesis and tectonic environment of their formation. Also, unlike previous studies that focused on the Damavand volcano and its eruption, the present study uses geochemical data to determine the origin of magmatism and the differentiation processes that occurred in this region.

Geology of the study area

The study area is situated within the Alborz Mountains and the eastern portion of the Central Alborz Zone, with coordinates ranging from 52°00′ to 52°35′ E and 35°15′ to 36°00′ N. Fig. 1b presents the incomplete stratographic sequence of Middle Cambrian to Late Cambrian rock units (Mila Formation) in the study area. These deposits consist of gray dolomite and red silt with red and white sandstone layers from bottom to top (Stoklin et al., 1964). The oldest Paleozoic rock units in the region are the Mobarak Formation. This formation consists of dark gray to black limestones with thin to thick layers, sometimes accompanied by biomicrosparite, biosparite, and bioclastic facies, with interbedded brachiopod fossils. Ruteh Formation (Permian unit) consists of limestone, shale, sandy lime, and sandstone with thin to medium layering. Lithologically, the Elika Formation (Triassic) is composed of fine-grained dolomitic limestone (vermiculite lime), oolitic gray lime, and gray to beige lime (Stocklin, 1972). The Lar formation consists of thin-layer micrite to massive (but dense) carbonates containing chert nodules or silicon layers (Aserto, 1966). In the sediments of this area, some pumice fragments and trachyandesite lavas of Damavand are visible. According to Hassanzadeh et al., (2001), these deposits indicate the release of trachyandesites before the alkali-olivine basalts.

The Tizkooh Formation (Upper Cretaceous) at the base has red soils and iron-bearing deposits (Pisolite). Then, it extends with yellow clastic limestones featuring red conglomerate layers, and finally ends with Orbitolina-bearing fine-grained limestones and thick limestones containing Rudist and Gastropods (Darvishzadeh, 2004). The Fajan Formation (PEf), with a thickness of approximately 1,500 m, is made up of polygenetic conglomerate, red sandstones, sandy marls, agglomerates, and andesitic lavas (as interlayers) (Darvishzadeh, 2004). The relative age of this formation is from the Paleocene to the Lower Eocene. Additionally, the Ziarat Formation (PEz) comprises gypseous marls and thick, layered limestones, featuring masses of nummulites, discocyclines, and bivalve fossils. This formation, with a Lower Eocene age, is located on the Fajan Formation and under the green tuffs of Karaj (Darvishzadeh, 2004). The oldest phase of volcanic activity is associated with Pulor basalts (Fig. 2a), whereas trachyandesitic to trachyte rocks (Fig. 2b) formed in more recent phases (Darvishzadeh, 2004).

Study method

In this study, 70 samples were collected during field operations, and then their thin sections were prepared and examined. The amount of major, minor, and trace elements in the region was determined by selecting 15 samples of total rock and analyzing them using inductively coupled plasma mass spectrometry (ICP-MS).
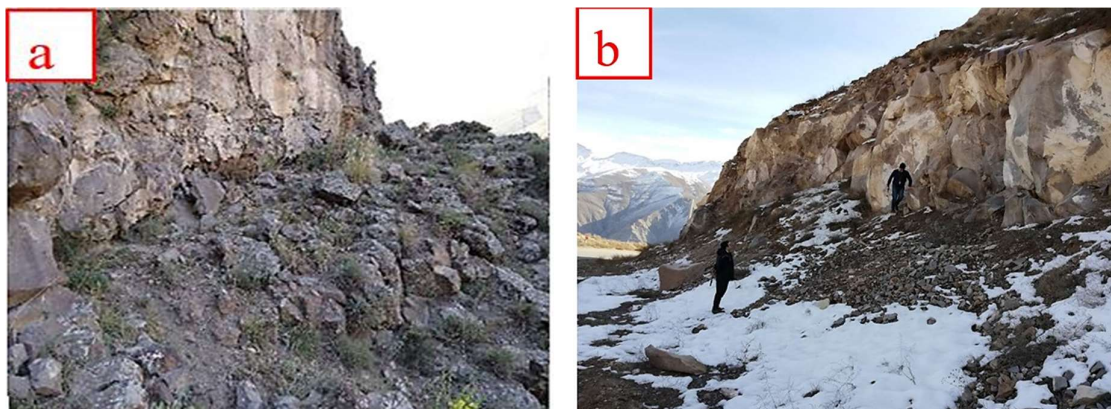
Figure 2. a) A view of basaltic lavas near the village of Pulor (looking south) and b) A view of Thracian andesitic lavas north of the village of Rineh

Major elements were analyzed using X-ray fluorescence spectrometry (XRF) at Kansaran Binalood and Zar Azma Company, Iran. The detection limit is 0.05% for major elements and LOI, 0.01 ppm for Tb, 0.02 ppm for Dy and Sm, 0.05 ppm for Er, Gd, Ho, Pr, and Yb, 0.1 ppm for As, Cd, Ga, Ta, Th, U, Eu, Lu, and Tm, 0.5 ppm for Ce, Hf, Sc, Y, and Nd, 1.0 ppm for Ba, Co, Cr, Cu, La, Nb, Ni, Pb, Rb, Sr, V, W, and Zn, and 5.0 ppm for Zr. The uncertainty of the measurements using internal laboratory standard materials falls within the 95% confidence interval with a coverage factor of k = 2.

Petrography

The thin sections of the igneous rocks consist of olivine basalt, basaltic trachyandesite, and trachyandesite, which will be examined in the following sections.

Olivine Basalt

The olivine basalts of the region have a gentle slope to the north, and the lavas are located between the discontinuous alluvial units of the Haraz River and its tributaries. The dominant texture in these volcanic rocks is porphyritic with a microlithic background, representing two stages of magma crystallization (Jackson, 1970). Their macrocrystals are mostly of the olivine (5-10%), clinopyroxene (15-20%), and plagioclase (35-40%) types. Olivine macrocrystals are semi-morphological to bimorphological and are rarely observed as automorphs. Abundant fractures in these minerals have caused their transformation into idingsite. Clinopyroxene (augite) macrocrystals are often morphological to semi-morphological. Plagiocalce crystals in the form of phenocrysts are of low abundance compared to other minerals in the rocks. In the studied rocks, plagiocalce microliths comprise a significant portion of the background. The matrix is composed of plagioclase, diopside (pyroxene), olivine, and opaque minerals. Most of the mafic minerals in the matrix have been replaced by opaque and calcite minerals in these samples. Minor minerals include euhedral to anhedral monocrystalline opaque and anhedral to subhedral biotites dispersed in the rock matrix.

Basaltic trachyandesite

These rocks are observed in hand samples in gray to dark gray. The texture of these rocks is porphyry and microlithic. In the modal composition, plagioclase, clinopyroxene, potassium feldspar (sanidine), phlogopite, and opaque and glassy minerals are present. Plagioclase

minerals, which comprise about 50 vol.%, generally have a size of less than 1 mm, ranging from microlite to larger grains, and exhibit polysynthetic twinning and composite zoning. Albite-periclinal and albite-carlsbad twinning are among the main features of plagioclases. Based on optical properties and refractive index, the range of plagioclases is from labradorite to anorthite. In this plagioclase, non-equilibrium textures such as sieve texture and oscillatory zoning are observed. Augite-type pyroxene is found in the rock texture, with an abundance of 17-22 vol.% in the form of automorphic to amorphous crystals, and in some cases with twinning. Phlogopite is found in the rock texture with an abundance of less than 10 vol.%, typically in the form of automorphic to flaky crystals, and is often altered. One of the main inclusions in these phlogopites is apatite (Fig. 3a). Amphiboles are semi-amorphous to amorphous, and in most cases are strongly altered. The background consists of plagioclase microlites, alkali feldspar, pyroxene, and opaque and glassy minerals (Figs. 3b and 3d).

Basaltic Thracian andesite highly rich in biotite

In hand specimens, they appear dark gray, with fine crystals or no crystals at all. They have a porphyry texture with microlithic and trachytic textures. The plagioclases, which exhibit polysynthetic twinning, decompose into calcite, chlorite, and albite at the surface. Based on the extinction angle, the measured plagioclases are andesine-oligoclase (An28-34). They also constitute 32 to 35 vol.% of the rock matrix. Some of the plagioclases are degraded from the center outward, exhibiting a zoning structure. Biotite crystals are often amorphous to semi-amorphous with direct extinction. They have inclusions of other minerals, such as opaque or iron oxides. Alkali feldspars (Afs) are found as euhedral (elongated) phenocrysts and microcrystals in the matrix. This mineral constitutes approximately 15% of the rock in cross-section. Pyroxenes are found in microcrystalline sizes. They are of the augite type and constitute 7 vol.% of the rock in thin sections. Amphiboles (Am) are amorphous to amorphous in form with relatively moderate abundance (Fig. 3c). Iron oxides or opacities are accessory minerals of these rocks. Secondary minerals of this rock include calcite, chlorite, and iron oxides formed by the decomposition of plagioclase and mafic minerals (Fig. 4a). The characteristics of these amphiboles include the very intense alteration of these minerals and opacities at the margins. In addition, the alteration products of these minerals include biotite and opacities. The matrix consists of plagioclase, alkali feldspar, pyroxene, and opaque minerals. In these samples, most of the mafic minerals in the matrix have been replaced by opaque minerals.

Petrographic evidence of magma mixing and contamination in rocks of the region

Oscillating zoning in plagioclase

Although plagioclase is the most prevalent mineral in the region's rocks, some zoning is evident (Fig. 2d). The factors that influence the degree and normal or reverse zoning in plagioclases are dependent on physical parameters such as temperature (T), total pressure (P), and melt water content (H_2O wt.%) (Singer et al., 1995; Kersse & Ghiorso, 2004). According to Ustunisik et al., (2014), three processes have been proposed within the basic system:

Two-stage crystallization process: In the first stage, magma ascends from a deeper chamber to a shallower one, where it crystallizes plagioclase at lower pressures. In the second stage, magma accumulates in the shallower chamber and continues to crystallize isobarically. If these two stages are repeated, the outcome is the development of reverse, normal, and oscillatory zoning in plagioclase.
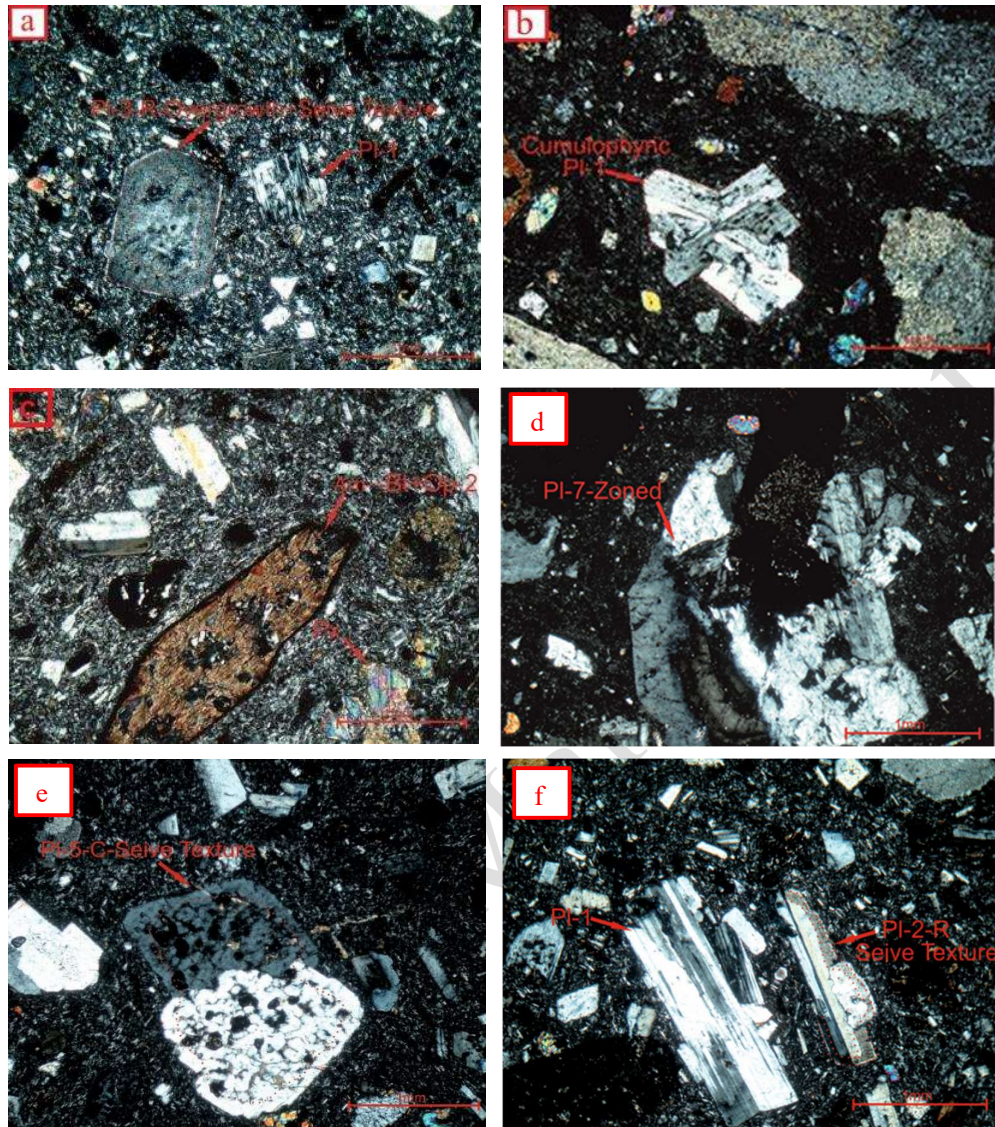
Figure 3. a) A view of sieve texture in basaltic trachyte andesite; b) A view of plagioclase phenocryst without non-equilibrium texture and with glomeroporphyritic texture (Pl-1) (red dotted line) in the matrix of the basaltic trachyte andesite rock; c) A view of subhedral hornblende phenocrysts replaced by biotite and opaque and pyroxene minerals in basaltic trachyandesite; d) A view of plagioclase phenocrysts with complete oscillatory zoning texture of the basaltic trachyte andesite rock; e) A view of a plagioclase phenocryst with a sieve-type disequilibrium texture within a plagioclase mineral; and f) A view of a plagioclase phenocryst without disequilibrium texture and a plagioclase phenocryst with a sieve-type disequilibrium texture

Plagioclase zoning in a large, convective magma chamber: In this process, plagioclase crystallizes simultaneously with magma convection, leading to oscillatory zoning.

A two-stage process interrupted by multiple recharge events: In this scenario, magma crystallizes isobarically as a new batch of primary magma is periodically injected into the magma chamber, and crystallization continues after mixing. During the repetition of these two stages, plagioclase develops normal and reverse zoning.

Notably, the Damavand volcano has numerous crystallized and semi-crystallized magma reservoirs at different depths (Mostafanejad et al., 2011; Shomali & Shirzad, 2014; Eskandari et al., 2018). Therefore, the magma mixing process might have occurred in the plagioclase rocks

of the region, in some cases with a dissolution margin. As a result, magma has been injected from lower to upper reservoirs, disrupting the physical and chemical balance in the magma reservoir.

Plagioclase with a sieve texture and dusty margin

Plagioclase with sieve texture and dusty margin: Fine and coarse sieve texture is observed in the core and margin of the crystal, along with growth and sometimes dissolution margin in plagioclases (Figs. 2e and 2f).

In general, honeycomb or sieve textures are the effects of melting and subsequent dissolution during magmatic mixing (Kuo, 1950; Sigurdsson, 1971; Eichelberger, 1978). Also, the presence of sieve texture in the center of the crystal indicates that there was a reaction and contact between mafic and acidic magma (Eichelberger, 1978; Hibbard, 1981; Humphreys et al., 2006; Perugini & Poli, 2012). Also, the fine-sieve texture at the edge of the crystal is associated with the injection of primary magma into the reservoir, magmatic temperature increases, and its mixing with the remaining magma and partial dissolution and contact of the crystal with calcium-rich magma (Viccaro et al., 2010; Coote & Shane, 2016; Renjith, 2014) in the reduction process. When the water-saturated magma rises rapidly, the water vapor pressure in the system increases, causing instability in the plagioclase crystal, which leads to dissolution and the formation of a sieve texture (Renjith, 2014). Viccaro et al., (2016) attribute the fine sieve texture at the edge of the plagioclase crystals to the injection of mafic magma and magmatic mixing. They also point out that when the magma rises to the surface, the reduction in pressure and the presence of undissolved water molecules in the melt contribute to the dissolution of the plagioclase.

In some macrocrystals, a coarse-sieve texture is seen across the entire crystal surface, sometimes accompanied by a dissolution rim. Therefore, these crystals can be considered a sign of rapid magma movement and possibly subsequent eruption. The lack of evidence of growth at the crystal edge supports this interpretation. In some macrocrystals, a thin rim features fine-scale oscillatory zones, which may indicate that stable conditions were reached after rapid transport and pressure reduction before eruption. According to Nelson & Montana, (1992) the formation of a coarse sieve texture is best attributed to conditions of rapid magma ascent followed by rapid pressure reduction. These researchers demonstrated that magmatic mixing alone cannot account for the formation of a coarse sieve texture. In fact, the effect of rapid pressure reduction in the formation of a coarse sieve texture is much greater than that of magmatic mixing or temperature increase.

According to textural evidence, the crystals in the magma reservoir were crystallizing in a melt that underwent successive changes in temperature, water vapor pressure, and chemical changes.

Corrosion of crystals

Dissolution occurs when a crystal in the magma moves away from its stable condition. This instability can be caused by factors such as changes in pressure, temperature, or the chemical composition of magma (Chen et al., 2016). Due to heating and melting basaltic olivine rocks, some researchers have attempted to determine the mechanism behind the formation of rounded and bay-shaped crystals (Banks & Burrett, 1989).

Amphibole

The amphiboles in the rocks of the region have signs of melt-crystal disequilibrium. As mentioned, the amphiboles in these rocks exhibit an opacity boundary (Fig. 3c). As a result of

thermodynamic instability in open systems, amphibole minerals have broken down and turned into a set of pure Oxide minerals (magnetite and hematite), Clinopyroxenes devoid of iron, Sphene, and Feldspars. This process can affect parts of the margin and even the whole mineral. Amphiboles are sensitive to changes in water, temperature, and pressure, and the imbalance of these minerals is a result of pressure changes during ascent and temperature changes at the time of occurrence. Magmatic mixing takes place (Browne & Gardner, 2002; Gill, 2010).

Plagioclase mineral chemistry

Plagioclase is the most abundant mineral in the region's rocks, occurring in two forms: Phenocrysts and Microlites. The petrographic evidence indicates moderate alteration in these plagioclases. As a result, secondary minerals such as sericite, calcite, chlorite, and clay minerals, along with securitization, can be observed on them. In this research, 4 suitable thin-polished sections were selected from the outcrops of the region and were analyzed using a Cameca SX 100 electron microprobe at Kansaran Binaloud Company, Iran. On the Or-Ab-An triangle diagram from (Deer et al.,1991), the plagioclase of the igneous rocks of the region is placed in the range of labradorite and bitonite (Fig. 4). Table 1 shows the type of plagioclase rocks of the region using a Spreadsheet. The increase in water vapor pressure, the sudden ascent of magma, and the creation of magmatic imbalance conditions respectively decrease the amount of anorthite and increase the amounts of Fe and Mg in plagioclase (Ahmadi et al., 2017).

Geochemistry of the rocks

In the diagram proposed by (Lebas et al., 1986), classification is performed based on total alkali-silica (TAS) parameters. According to this diagram, the volcanic rock samples in the Polur region fall within the range of basaltic trachyandesite and trachyandesite (Figs. 5a and 5b). According to (Pearce, 1982), the samples of the study area fall within the range of the Shoshonitic series (Fig. 5c).

Table 1. Major element abundances (wt.%) of the plagioclase

|	R27	R27	R27	R15	R15	R15	R18	R18	R18	P3	P4	P5
SiO_2	61.68	64.59	64.02	54.63	59.74	58.25	52.64	52.68	53.11	54.44	53.43	52.78
TiO_2	0.23	0.14	0.28	0.31	0.33	0.26	0.03	0.05	0.07	0.06	0.06	0.06
Al_2O_3	18.76	18.75	17.61	17.57	17.84	20.04	27.96	27.89	28	27.41	28.2	28.38
Fe_2O_3	0.76	0.74	0.85	1.11	1.32	0.98	0.65	0.54	0.61	0.69	0.74	0.72
CaO	5.73	5.77	5.08	13.46	7.86	12	13.69	14.49	13.61	12.09	13.07	13.57
Na_2O	5.53	3.05	4.07	5.2	5.8	5.43	3.53	3.55	3.59	4.5	3.77	3.62
K_2O	5	5.43	5.77	3.49	5.29	1.57	0.09	0.1	0.08	0.17	0.21	0.13
MgO	0.04	0.03	0.03	0.09	0.09	0.06	0.12	0.16	0.19	0.14	0.13	0.18
MnO_2	0.17	0.11	0.16	0	0	0	0.02	0	0.02	0	0.02	0.01
Cr_2O_3	0	0	0	0.21	0.42	0.1	0	0	0.02	0	0.02	0.01
P_2O_5	0	0	0	2.64	0.07	0.02	0	0	0	0	0	0
Si	11.46	11.76	11.82	10.70	11.24	10.82	9.71	9.68	9.74	9.93	9.76	9.68
Ti	0.03	0.02	0.04	0.05	0.05	0.04	0.00	0.01	0.01	0.01	0.01	0.01
Al	4.11	4.02	3.83	4.06	3.96	4.39	6.08	6.04	6.05	5.89	6.07	6.13
Fe(ii)	0.12	0.11	0.13	0.18	0.21	0.15	0.10	0.08	0.09	0.11	0.11	0.11
Ca	1.14	1.13	1.00	2.82	1.58	2.39	2.71	2.85	2.67	2.36	2.56	2.67
Na	1.99	1.08	1.46	1.97	2.12	1.96	1.26	1.26	1.28	1.59	1.33	1.29
K	1.19	1.26	1.36	0.87	1.27	0.37	0.02	0.02	0.02	0.04	0.05	0.03
TOTAL	20.04	19.38	19.64	20.65	20.43	20.11	19.89	19.94	19.87	19.93	19.89	19.91
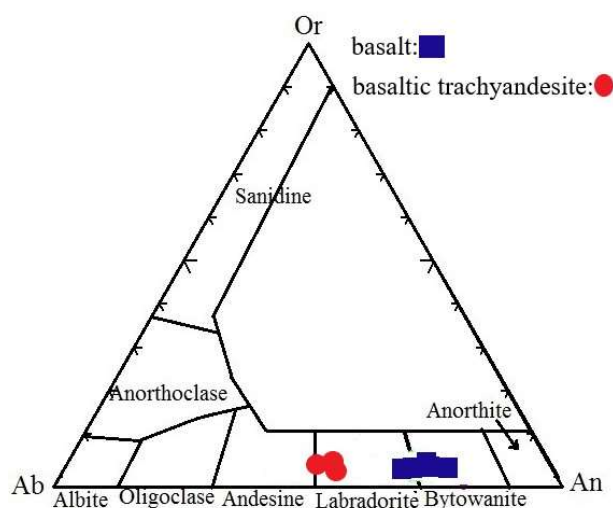
Figure 4. Determining the composition of feldspars of igneous rocks using the diagram proposed by (Deer et al., 1991)

Table 2. The type of plagioclase rocks of the region

Point.No	An	Ab	Or
Ba-r27-1	26.42	46.14	27.45
Ba-r27-2	32.50	31.09	36.41
Ba-r27-3	26.30	38.13	35.57
An-R15-1	39.80	44.82	15.38
An-R15-2	31.88	42.57	25.55
An-R15-3	50.64	41.47	7.89
Tr-An-R18-1	67.82	31.65	0.53
Tr-An-R18-2	68.89	30.54	0.57
Tr-An-R18-3	67.37	32.16	0.47
Ba-P3-1	59.16	39.85	0.99
Ba-P3-2	64.89	33.87	1.24
Ba-P3-3	66.93	32.31	0.76

Table 3. Whole rock geochemical compositions of the volcanic rocks of Haraz road (major elements in wt.%, trace and rare earth elements in ppm)

No	P10	P3	P8	P14	P7	P12	P13	T5	R8	R27	R18	R15	R24	R3	R4	R12	R28	R5A
SiO_2	63.63	50.99	51.70	50.35	52.34	51.21	50.92	58.93	61.95	62.42	62.24	62.34	62.07	62.02	62.81	62.42	61.12	62.72
Al_2O_3	13.66	12.75	13.08	12.76	13.01	13.00	12.62	17.00	16.25	16.10	15.96	16.05	16.21	16.04	16.04	15.68	16.25	16.18
BaO	0.15	0.23	0.19	0.22	0.20	0.26	0.23	0.16	0.15	0.14	0.14	0.14	0.14	0.13	0.13	0.14	0.15	0.14
CaO	4.33	8.94	9.21	8.48	8.81	8.65	8.46	4.86	4.05	3.88	4.01	3.88	4.00	4.84	3.97	4.16	4.20	3.93
Fe_2O_3	2.47	3.44	3.35	3.44	3.44	3.48	3.47	2.67	2.49	2.44	2.45	2.43	2.45	2.41	2.42	2.45	2.53	2.42
FeO	2.37	4.80	4.81	4.83	4.97	4.86	5.46	2.96	2.23	1.98	2.05	1.97	2.10	1.98	2.05	2.06	2.36	2.05
K2O	4.46	1.98	2.24	3.67	1.70	2.19	2.40	4.22	4.23	4.46	4.40	4.50	4.37	4.27	4.37	4.45	4.27	4.31
MgO	2.63	8.72	8.23	8.71	8.10	8.59	8.65	2.51	2.31	2.21	2.35	2.32	2.29	2.12	1.98	2.26	2.56	2.07
MnO	0.08	0.13	0.13	0.13	0.14	0.13	0.13	0.07	0.07	0.07	0.07	0.07	0.07	0.10	0.07	0.07	0.08	0.07
Na_2O	4.58	4.47	3.97	4.00	4.01	4.19	4.23	4.76	4.74	4.81	4.81	4.86	4.76	4.65	4.72	4.80	4.82	4.67
P_2O_5	0.61	1.60	1.23	1.43	1.33	1.43	1.44	0.67	0.48	0.49	0.52	0.48	0.53	0.47	0.47	0.54	0.59	0.46
SO_3	0.07	0.05	0.07	0.05	0.07	0.07	0.07	0.05	0.05	0.06	0.05	0.05	0.05	0.08	0.05	0.05	0.05	0.05

TiO$_2$	0.96	1.89	1.80	1.92	1.88	1.93	1.93	1.15	0.99	0.93	0.95	0.92	0.95	0.88	0.92	0.94	1.02	0.92
LOI	0.52	2.44	2.46	0.59	2.91	2.01	1.68	0.91	0.21	0.21	0.25	0.38	0.19	1.04	0.22	0.21	0.25	0.23
Ag	0.62	0.41	0.52	0.45	0.53	0.70	0.46	0.33	0.51	0.50	0.43	0.32	0.47	0.29	0.47	0.42	0.30	0.47
As	5.00	9.00	3.00	2.00	7.00	16.00	7.00	2.00	3.00	3.00	3.00	7.00	6.00	5.00	6.00	5.00	7.00	7.00
Ba	1310	1740	1548	1848	1569	2066	1904	1295	1212	1206	1225	1111	1217	1118	1148	1211	1329	1172
Be	3.43	2.34	2.13	2.45	2.15	2.37	2.47	2.67	3.36	3.84	3.79	3.48	3.93	3.43	3.57	3.87	3.94	3.59
Bi	0.06	0.05	0.07	0.07	0.07	0.08	0.06	0.05	0.06	0.11	0.04	0.04	0.04	0.05	0.04	0.04	0.07	0.04
Cd	0.46	0.48	0.78	0.57	0.95	0.98	1.11	0.76	0.17	0.20	0.20	0.44	0.20	0.26	0.39	0.16	0.16	0.40
Ce	141.40	207.20	177.80	215.60	154.00	208.60	198.80	129.64	138.18	119.70	123.62	107.94	124.88	109.34	107.80	121.94	131.88	107.66
Co	2.58	7.91	8.29	5.80	5.23	5.22	7.77	0.72	0.80	0.24	0.80	0.84	0.71	1.88	0.96	0.20	0.55	0.60
Cr	49.00	126.00	171.00	144.00	168.00	166.00	174.00	49.00	31.00	27.00	28.00	25.00	30.00	30.00	33.00	29.00	32.00	32.00
Cs	1.41	1.14	1.30	1.23	1.40	1.28	1.22	1.47	2.23	1.45	1.77	2.07	1.94	1.84	1.73	1.55	2.33	1.69
Cu	12.30	30.10	36.70	39.60	25.50	32.40	27.10	23.90	18.10	9.40	12.90	11.00	13.90	13.50	10.40	19.40	18.50	8.50
Dy	2.54	3.50	3.32	3.76	3.35	3.64	3.56	2.27	2.65	2.00	2.06	1.82	2.10	2.04	2.07	2.02	2.26	2.07
Er	1.03	1.29	1.28	1.40	1.27	1.36	1.31	0.94	1.12	0.90	0.90	0.81	0.87	0.86	0.99	0.87	0.93	0.93
Eu	3.08	4.40	3.88	4.63	3.94	4.75	4.26	2.76	3.15	2.59	2.61	2.38	2.64	2.46	2.50	2.53	2.75	2.46
Fe	34667	49348	54937	56095	54478	57544	57404	36584	32333	29455	29772	25514	29445	28282	28835	29905	32880	29790
Gd	6.66	9.52	8.36	10.00	8.50	9.60	9.06	5.85	6.41	5.35	5.43	4.79	5.58	5.12	5.11	5.44	5.98	5.12
Hf	6.62	2.16	3.90	2.67	3.71	4.18	3.09	4.10	6.29	5.73	5.31	4.69	5.89	3.94	5.46	4.99	3.82	5.33
Ho	0.56	0.65	0.65	0.68	0.65	0.67	0.65	0.53	0.65	0.51	0.51	0.49	0.51	0.51	0.52	0.51	0.52	0.52
In	0.03	0.02	0.02	0.03	0.02	0.03	0.02	0.01	0.05	0.03	0.07	0.01	0.08	0.01	0.05	0.03	0.02	0.04
K	19924	11154	13705	19156	11721	15398	14790	21632	24314	23380	19420	30570	31644	28262	31534	23979	22598	31090
La	79.38	93.10	80.64	97.16	80.92	93.80	90.02	74.90	79.24	68.18	70.42	61.74	70.70	63.00	61.74	70.28	73.08	60.76
Li	15.00	9.00	14.00	7.00	13.00	10.00	10.00	10.00	18.00	14.00	16.00	15.00	18.00	18.00	12.00	18.00	17.00	11.00
Lu	0.16	0.16	0.16	0.17	0.17	0.17	0.16	0.15	0.19	0.15	0.15	0.14	0.15	0.15	0.15	0.15	0.15	0.15
Mg	14739	40423	42550	45047	41146	44090	45856	12906	12416	11610	11775	10653	11930	11147	10671	11999	13866	11065
Mn	500.00	805.00	929.00	927.00	892.00	906.00	920.00	450.00	473.00	425.00	453.00	425.00	472.00	499.00	455.00	486.00	557.00	465.00
Mo	2.35	0.01	1.22	2.25	0.53	1.89	0.92	1.47	3.19	6.03	4.22	4.51	3.14	1.54	2.83	3.55	3.16	3.76
Nb	0.47	0.74	0.19	0.44	0.84	0.96	0.41	0.20	0.71	0.83	0.54	0.63	0.30	0.21	0.73	0.10	0.30	0.63
Nd	40.37	51.16	42.69	54.06	51.04	51.50	50.23	37.35	39.09	32.83	32.71	29.00	34.57	30.51	29.70	33.06	36.89	30.28
Ni	40.00	173.00	188.00	198.00	185.00	195.00	206.00	37.00	14.00	15.00	16.00	12.00	27.00	13.00	11.00	16.00	18.00	16.00
P	2561	3942	4184	3850	4354	3380	4410	2657	2009	1995	2050	1854	2163	1861	1930	2166	2529	1876
Pb	13.55	17.79	14.26	9.44	6.92	19.73	4.13	13.20	15.84	42.68	18.28	22.98	12.44	13.28	13.45	12.22	12.94	9.98
Pr	14.70	20.30	17.22	21.14	17.50	20.44	19.74	13.50	14.28	12.32	12.60	11.06	12.78	11.40	11.26	12.50	13.83	11.16
Rb	183.00	295.00	262.00	298.00	269.00	307.00	280.00	190.00	175.00	155.00	156.00	141.00	161.00	139.00	133.00	159.00	203.00	138.00
S	126.00	157.00	36.00	135.00	30.00	173.00	52.00	210.00	90.00	217.00	106.00	15.00	20.00	110.00	41.00	100.00	119.00	46.00
Sb	2.64	2.98	2.96	3.00	3.00	2.90	2.93	2.73	3.25	2.62	2.58	2.62	2.51	2.58	2.45	2.60	2.56	2.47
Sc	6.70	13.40	15.60	14.90	15.50	14.80	15.30	7.80	6.20	5.30	5.50	4.40	4.90	5.50	5.30	5.40	6.40	5.40
Sm	8.97	13.34	11.47	13.97	11.62	14.00	12.85	8.04	8.76	7.25	7.38	6.48	7.55	6.97	6.99	7.21	8.08	7.06
Sn	0.03	0.02	0.06	0.04	0.02	0.03	0.03	0.01	0.06	0.08	0.04	0.03	0.04	0.03	0.09	0.07	0.03	0.01
Sr	1365	2116	1872	2066	1908	2059	2138	1567	1140	1238	1238	1087	1240	1089	1098	1308	1649	1101
Ta	6.10	0.38	1.11	0.86	1.62	0.42	0.86	4.18	6.70	5.53	5.49	5.49	5.42	6.26	5.94	5.94	5.59	4.17
Tb	0.78	1.07	0.96	1.12	0.98	1.10	1.04	0.70	0.76	0.64	0.65	0.59	0.66	0.64	0.64	0.63	0.71	0.64
Te	15.60	20.60	18.50	22.50	18.80	25.10	20.90	13.30	15.80	12.70	13.00	12.40	13.30	12.30	12.00	12.20	13.60	12.20
Th	19.43	6.67	7.20	7.29	7.30	7.21	6.83	12.65	20.90	20.10	18.76	14.74	18.63	14.61	17.69	17.55	12.03	17.69

Ti	6061	6504	9129	7849	9052	6809	8973	6137	5809	5328	5389	4966	5787	5352	5680	5529	6299	5691
Tl	0.36	0.33	0.35	0.35	0.35	0.35	0.34	0.34	0.49	0.36	0.33	0.32	0.32	0.33	0.37	0.34	0.32	0.37
Tm	0.18	0.18	0.19	0.19	0.19	0.19	0.18	0.18	0.22	0.17	0.17	0.17	0.17	0.17	0.18	0.18	0.17	0.18
U	4.74	2.10	2.02	2.20	1.91	2.17	2.10	3.29	5.05	4.72	4.46	3.50	4.39	3.67	4.04	4.28	3.29	4.18
V	78.00	125.00	146.00	143.00	150.00	142.00	150.00	88.00	77.00	66.00	66.00	61.00	74.00	58.00	75.00	69.00	82.00	73.00
W	1.32	0.16	0.02	0.07	0.09	0.14	0.01	1.41	1.75	1.78	1.72	1.81	1.58	1.01	1.90	1.41	1.18	1.76
Y	12.50	16.90	17.10	17.80	16.90	17.70	18.30	12.10	11.40	10.30	10.20	7.80	9.80	10.20	10.60	10.30	11.70	10.80
Yb	1.03	1.18	1.24	1.30	1.24	1.29	1.23	0.93	1.16	0.88	0.87	0.78	0.88	0.84	0.93	0.85	0.89	0.93
Zn	83.90	96.60	106.40	102.20	101.20	101.40	98.40	107.60	82.90	68.20	68.50	56.60	68.80	73.50	68.90	75.80	82.90	66.80
Zr	309.00	161.00	219.00	174.00	205.00	250.00	216.00	211.00	252.00	296.00	257.00	187.00	261.00	161.00	254.00	253.00	162.00	258.00
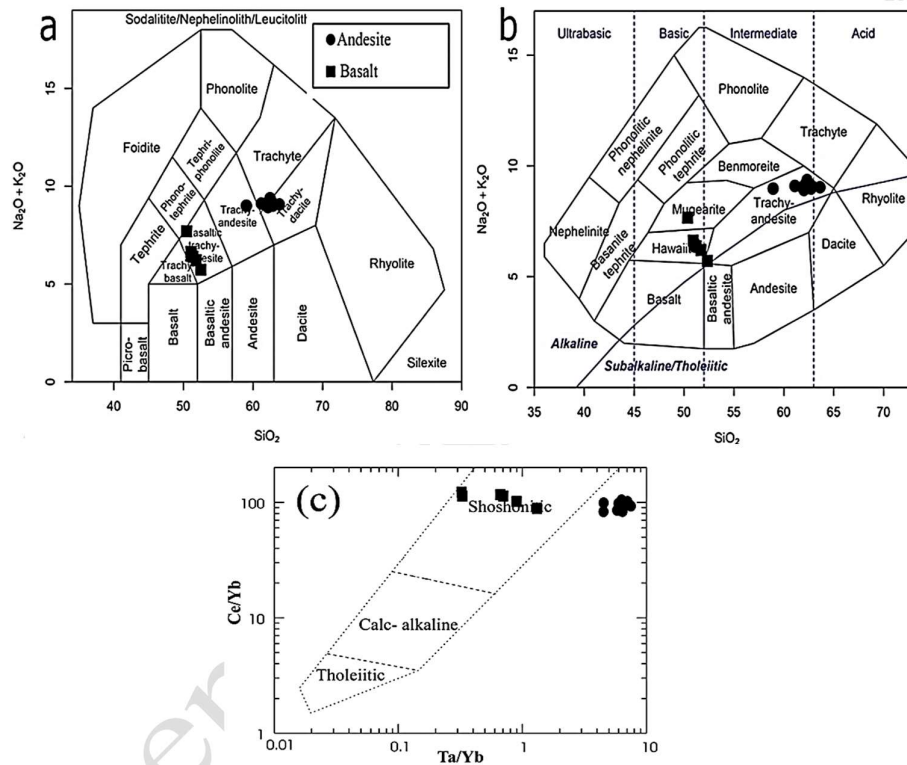
Figure 5. a) Diagram of middlemost, (1994); b) Diagram of SiO$_2$ Vs Na$_2$O+K$_2$O Cox et al., (1976); c) Ta/Yb vs. Ce/Yb; and d) Ta/Yb vs Th/Yb diagrams modified from Pearce, (1982)

As inferred from the spider diagram normalized to the OIB and Chondrites (Sun & McDonough, 1989), another prominent feature of the region samples is the highly fractionated patterns of rare earth elements (REE) (Figs. 6a and 6b). The low HREE values are due to the presence of garnet ± hornblende in the partial melting residue in the source area.

The existence of a linear and coherent pattern between trace elements observed in the chondrite diagram (Fig. 6b) suggests a common origin for these rocks. Also, it indicates that partial crystallization was the primary mechanism in their formation and evolution.

In Eu enrichment diagrams, it is observed that feldspars are usually the controlling factors of the Eu anomaly. Therefore, Eu^{2+} is associated with reducing conditions and is compatible in plagioclase and potassium feldspar minerals. The positive Eu anomaly can be explained by the fact that this element has accumulated in the residual melt. Therefore, Eu has a valence of +3 and has not entered the plagioclase mineral.
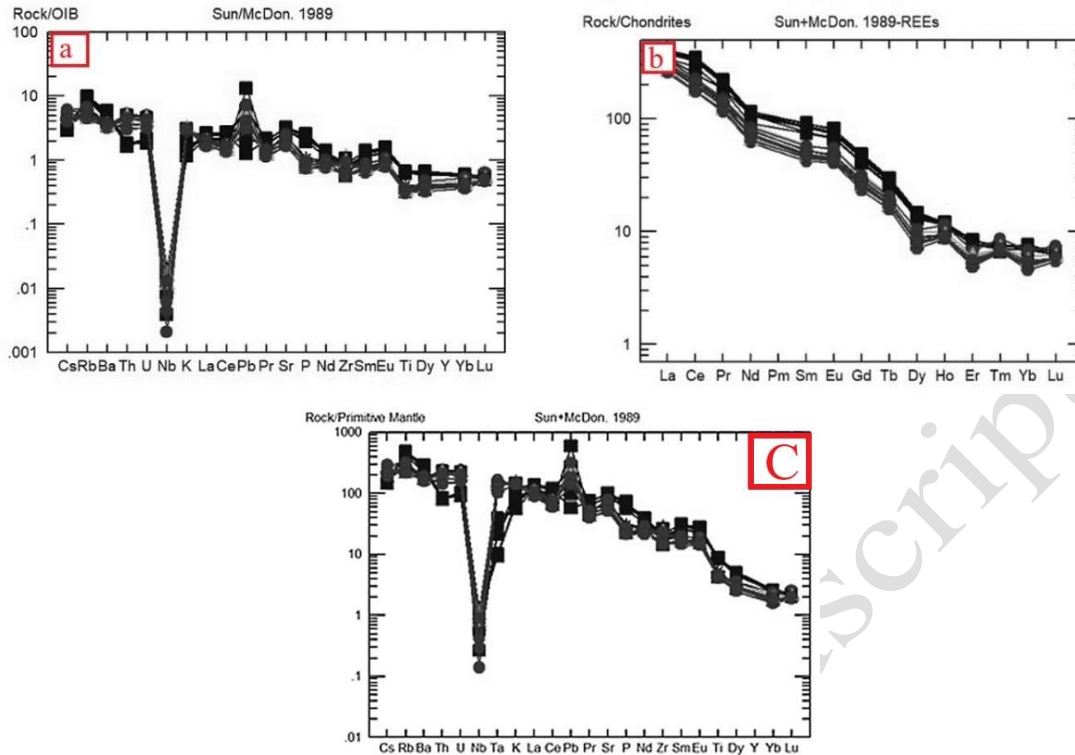
Figure 6. a) Normalized OIB spider diagram; b) normalized chondrite spider diagram; and c) Primitive mantle normalized trace element patterns for rocks of the study area

The depletion of Ta and Ti in the early mantle-normalized trace element diagram (Fig. 6c) in volcanic rocks indicates the fractionation of a titanium-rich phase in the magma source, which is unusual for upper mantle-derived magmas and appears to be due to subduction zone magmatism (Kuster & Harms, 1988; Wilson, 1989) or crustal-impregnated magmas (Rollinson, 1993). In addition, the stability of phases containing these elements during partial melting or their separation during magmatic segregation processes results in the depletion of these elements (Wu et al., 2003). A positive Pb anomaly is a prominent feature in all samples in the trace element diagram normalized to the early mantle composition (Fig. 6c). This feature may indicate crustal contamination of magma formed from partial melting of the mantle at higher levels (Kamber et al., 2002). On the other hand, the presence of a positive Pb anomaly and a negative Nb and Ta anomaly is indicative of magmas formed in volcanic arcs and magmas influenced by continental crust (Hofmann, 1988). Strong enrichment and positive anomalies of U and Th elements are also observed in all samples. Fan, (2003) noted that the strong enrichment of U and Th in spider diagrams suggests the addition of pelagic sediments or altered oceanic crust to the melting source. In Eocene volcanic rocks, Ti and Nb anomalies are clearly observed, which are attributed to other factors in addition to subduction magmatism:

It is a characteristic feature of continental crust rocks and participation in magmatic processes (Leutold et al., 2013; Rolinson, 1993).

The depletion of these elements in the origin is indicated by the stability of phases containing these elements during partial melting or their separation during the fractionation process (Wu et al., 2003).

In general, the patterns of the rare elements in alkaline basalts of Damavand in multi-element diagrams do not fully correspond to a tectonic environment and exhibit characteristics of both subduction and OIB environments. However, these rocks are more prone to OIB-like patterns. According to the Harker diagrams, most of the major oxides versus silica changes are relatively

continuous and highly correlated.

From alkaline basalts to trachyandesites, the concentration of K_2O increases, and MgO, Fe_2O_3, CaO, TiO_2, and MnO decrease (Fig. 6). These trends in proportion to the increase in silica can be attributed primarily to fractional crystallization. The strong negative correlation of MgO, Fe_2O_3, and MnO with SiO_2 can be due to the fractionation of olivine and pyroxene minerals in the early stages of magma crystallization. As SiO_2 increases, CaO also declines due to the fractionation of plagioclase and clinopyroxene. The TiO_2 versus SiO_2 diagram exhibits a downward trend for TiO2 because the Ti element can enter the structure of ferromagnesian minerals, such as pyroxene and hornblende, during the early stages of magmatic fractionation. The negative trend observed in the P_2O_5 versus SiO_2 diagram can also be attributed to the apatite crystallization process.
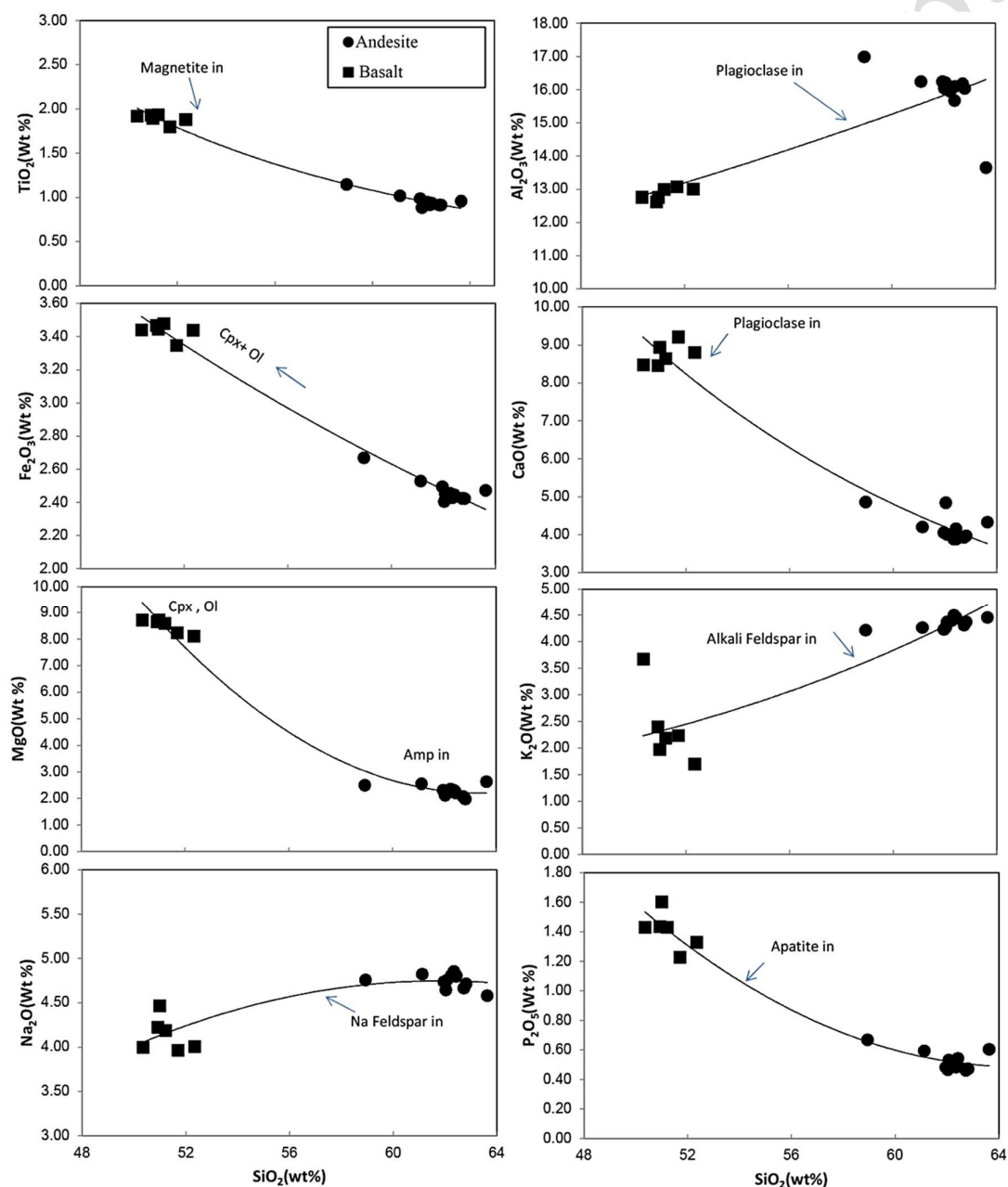
Figure 7. Harker diagrams

The examination of the Harker diagrams indicates a gap in correlation and coherence among the samples .Probably, the compositional break in the chemical evolutionary processes is a result of different origins in the magmas that produced the samples, or it depends on the type of magmatic transformation processes. (Dufek & Bachmann, 2010) showed that the absence of intermediate compounds, which is called the Daly gap, is common, and they explain this phenomenon by the separation of crystals and liquids during the intermediate stages of crystal separation, after which, in the complex Bimodal volcanisms that depend on crystal segregation, they do not produce magmas of intermediate composition. It should be mentioned that this density filtration is activated when the intermediate magmas are rich in iron and denser than the mafic and felsic magmas in the system (Christiansen & McCurry, 2008; McCurry et al., 2008).

Verma et al., (2006) introduced several diagrams to separate the tectonic environment of basaltic and ultrabasic rocks based on the logarithmic conversion of principal element ratios (Fig. 9a). In these diagrams, alkaline basaltic samples of the region are in the range of continental rift and OIB basalts.

According to Rollinson, (1993), the presence of scatter in the bivariate diagrams of compatible elements is an emphasis on magmatic mixing in the origin. According to Fig. 6, the strontium element exhibits an abnormal trend compared to the subtraction trend (i.e., a decreasing trend). This mode can indicate magmatic mixing, as abnormal trends are signs of new magma entering the magma reservoir and the magma mixing process (Winter, 2001). Additionally, microscopic examination of these rocks reveals evidence of magma mixing, including the sieve texture, the presence of two generations of healthy and altered plagioclases, and the reaction margin. According to this evidence, it can be concluded that magmatic mixing has played a significant role in the formation of volcanic rocks in the region. Bivariate diagrams related to pairs of elements selected from the group of incompatible elements can show the ratio of these elements in the origin of magma (Sun & McDonough, 1989). In general, the processes of magmatic mixing and crustal contamination cause changes in K/Rb-Ba/Rb and Zr/Rb ratios. These changes in crustal contamination are less sharp compared to magmatic mixing (Winter, 2001). When a bivariate graph of Rb is drawn against the mentioned ratios, contamination with the lower crust results in an increasing trend, while contamination with the upper crust yields a decreasing trend. However, in the presence of magmatic mixing, these ratios show drastic changes compared to pollution. According to the diagram of Zr/Rb for Rb (Fig. 8b), there is no specific correlation between volcanic rocks, and they exhibit a great dispersion. This state can be due to the injection of multiple magma pulses and magma mixing. It can be said that the most important processes that have played a role in the formation of volcanic rocks in the studied area are magmatic subtraction and mixing. Successive injections of primary magma originating from great depths into the lower crust and the injection of transformed alkaline basaltic magma to different depths in the upper crust cause uniformity in the chemical composition of lavas. Besides, it results in the lack of transformation of magma into more acidic compounds, despite the digestion of crustal rocks and their subsequent mixing. The ascent of basaltic magma stops in the middle levels of the upper crust due to the density difference between the crust and the melt, or a change in the tectonic regime. According to Eskandari et al., (2018), this stop occurred at a pressure of 6 to 8 kilobars, resulting in the formation of one or more magma reservoirs at depths ranging from 22 to 28 km. Probably, these reservoirs have been evolving for a long time without connection with higher depths. As a result, because the injection of basaltic magma accompanied the digestion of crustal rocks, the composition of the magma did not become more acidic.

According to Pearce, (1982), the diagram indicates that the rocks of the region fall within the range of within-plate basalts (WPB) (Fig. 9b). According to Davidson et al., (2004), the trachyandesites of Damavand are closely related to within-plate lava and do not overlap with island arc lava. These authors believed that a compressive regime existed outside the Damavand area, whereas the strike-slip stress regimes surrounding the volcano were younger and more active.
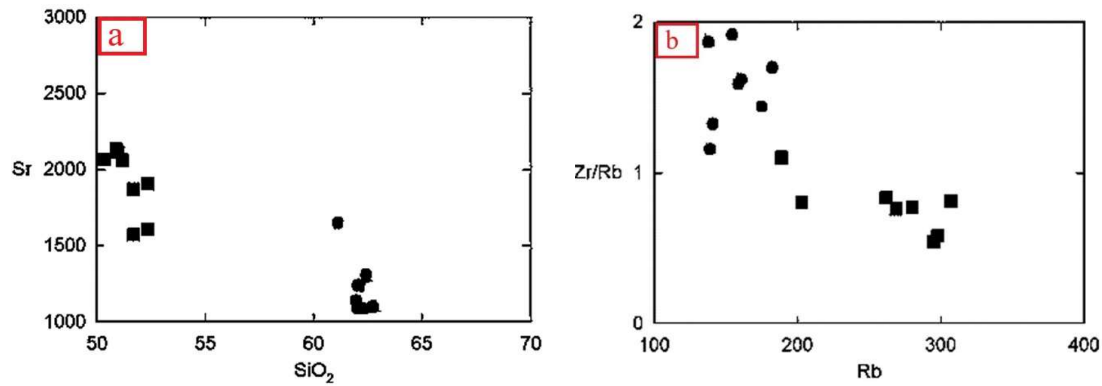
Figure 8. a) graph of SiO_2 versus Sr and b) graph of Rb versus Zr/Rb

Geotectonic diagrams for (ultra-)basic rocks of Verma et al. (2006)
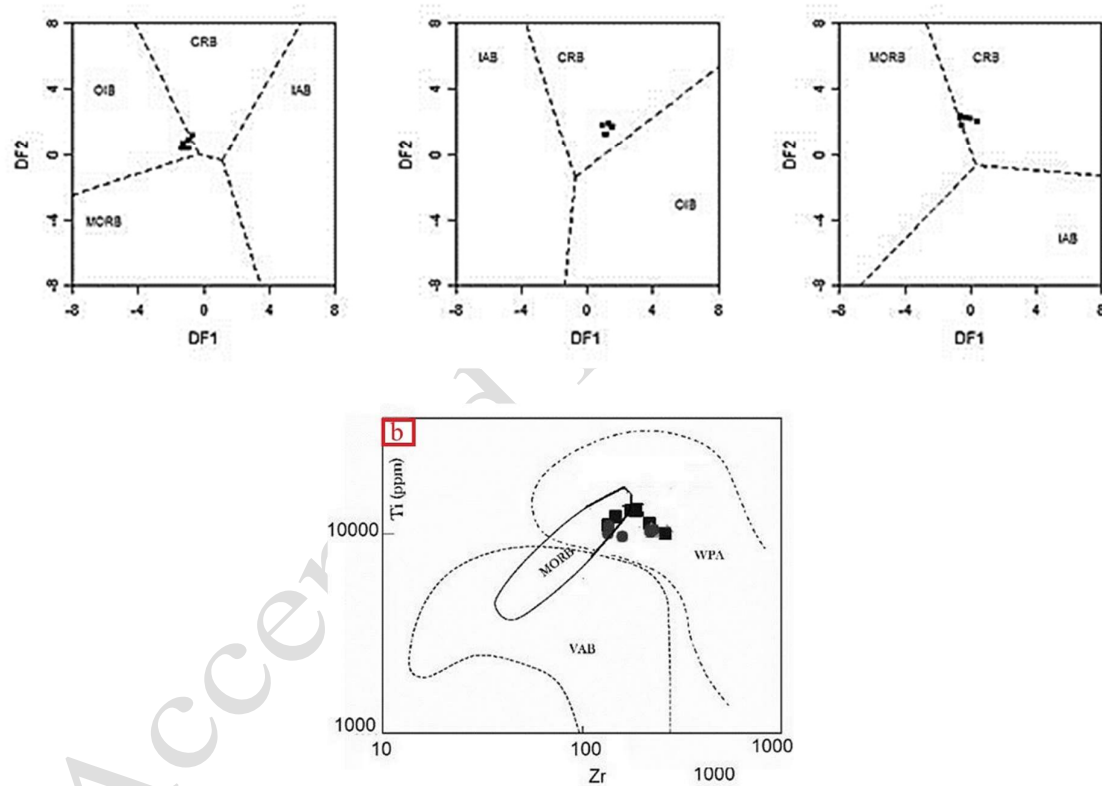

Figure 9. a) Diagrams of Verma et al., (2006) and b) Diagram of Pearce (1982)

As shown in Fig. 10a, the presence or absence of garnet in the mantle origin is detected by changes in the Sm/Yb ratio (Coban, 2007). The sensitivity of the distribution of REEs between the melt and the mantle source melt rock is high in the presence of garnet. HREEs, such as Yb, have a high distribution coefficient in garnet. Therefore, when garnet is present as a stable phase in the source rock, the HREE concentration in the melt will decrease. Thus, the Sm/Yb ratio in mantle partial melting in the presence of garnet is higher than in the absence of garnet (Fig. 7b). Hawkesworth et al., (1994) showed the changes in the ratios of Sm/Yb versus Ce/Sm. The ratio Sm/Yb = 2.5 is the criterion for separating the two garnet-bearing mantle and mantle without garnet ranges.
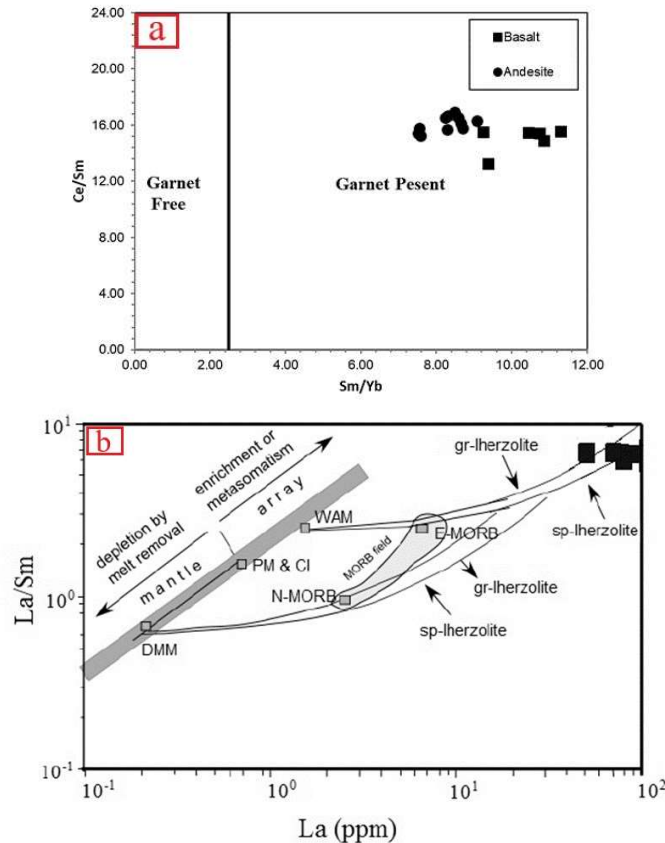
Figure 10. a) Diagram of (Coban, 2007) and b) diagram of La versus La/Sm taken from (Aldanmaz et al., 2006); as can be seen, the area's rocks are in the range of enriched mantle and the range of partial melting of Sp. Lherzolite

Based on Fig. 10a, the position of the studied rocks in the range of Sm/Yb> 2.5 indicates the equilibrium of the melt with the garnet-bearing mantle rocks (garnet-lherzolite). Lherzolite garnet is an index of the area with a pressure of 30 kbar and a temperature of more than 1300℃ from a depth of 60 to 80 km (McKenzie & Onions, 1991).

In some sources (e.g., Lustrino, 2005), a high Ce/Pb ratio has been introduced as one of the characteristics of the mantle source of oceanic island basalt (OIB) (Fig. 11a). As can be seen from the Ce/Pb versus CE diagram of Damavand's alkali basalts and the primitive magma, the rock samples are in the range of mantle MORB/ORB. However, some samples have a composition similar to that of continental crust due to contamination from their crust and an increase in their Pb content.

In the diagram of Th/Yb versus Ta/Yb, the basalt samples from the region fall within the OIB range, indicating an asthenosphere origin and a degree of enrichment. Meanwhile, other samples are outside the crystallization range and outside the partial crystallization range. Therefore, they indicate contamination of continental crust with previously enriched materials due to subduction or the materials that remained from pre-Quaternary subduction.

Another important indicator of crustal contamination is the high Ba/Zr ratios. In continental basalts contaminated with crust, this rate varies between 2 and 0 (Huang & Flower, 1998). The average of this ratio is in the basalts of the region. High levels of K/Nd (more than 300) may also result from crustal contamination. This ratio in the Damavand basalts has a wide range, from 168 to 398 (with an average of 300). These ratios can be influenced by other processes, in addition to crustal contamination, and indicate the recycling of crustal materials at the source

(Lustrino, 2005). The Th, U, Sr, Ba, and Pb enrichment pattern, along with the high Th/La ratios and low Sm/La ratios, should be attributed to source contamination with crustal materials, rather than crustal contamination. According to Fig. 10b, the presence of strong lead anomalies in such samples may suggest contamination of the source with crustal material (Taylor & McLenn, 1985). The variation range of Th/U, Nb/U, Ba/Nb, and Ce/Pb, along with other properties of alkaline olivine basalts, shows the presence of recycled material from the crust in the source area. This material is obtained from the participation and recycling of subducted sediments into the upper mantle during subduction (Perlovich et al., 2013). Turner et al., (1996) presented the Rb/Ba versus Ti/Y diagram to investigate the phenomenon of crustal contamination. The diagram illustrates the position of the lower (Lc) and upper (Uc) crust. The Lamproite range is considered the magma resulting from low partial melting and in equilibrium with the garnet-bearing mantle. The MORB range is considered to be the magma resulting from the asthenosphere (Fig. 10c).

The studied samples show a linear trend from the lower crust (Lc) to the upper crust (Uc). The enrichment of these rocks with LILE elements can be considered a result of crustal contamination. These samples show a linear trend from the lower crust (Lc) to the upper crust (Uc). Crustal contamination can be considered the cause of the enrichment of the Talkheh Rud sub-volcanic mass from LILE elements.

Techno-magmatic environment

Based on isotopic geochronology, this volcano was active in several stages from 1.8 million to 7300 years ago. Many hypotheses have been proposed about the geodynamics and formation of Damavand.
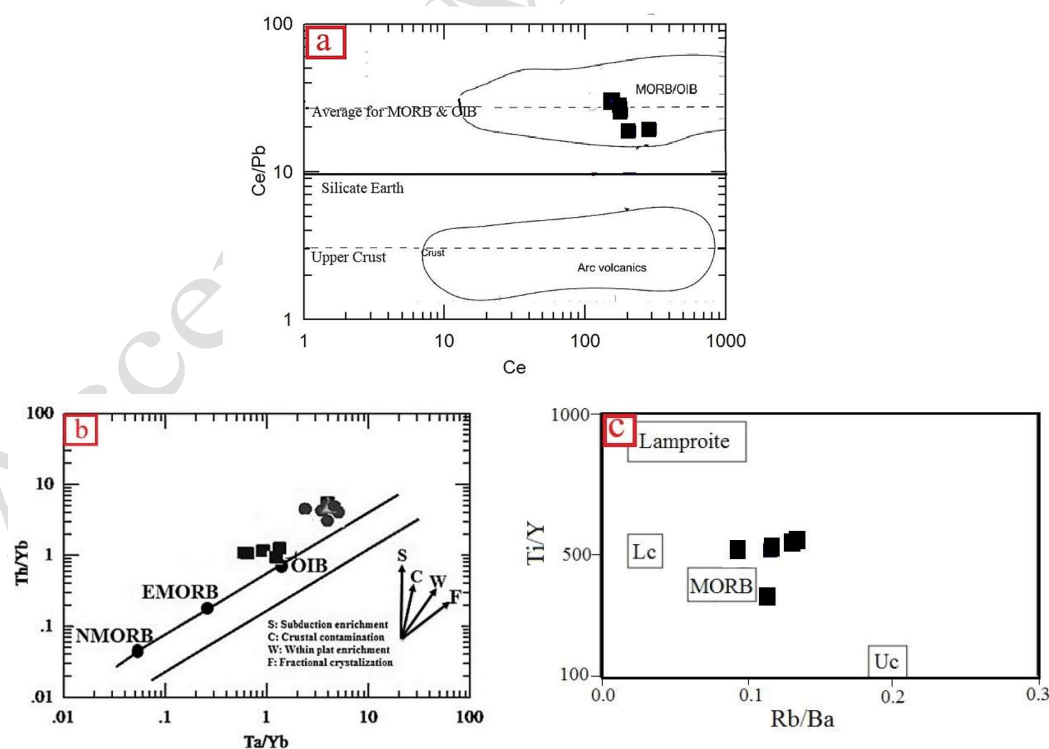

Figure 11. a) Diagram of Ce/Pb versus Ce to identify the origin of volcanic rocks; b) Diagram of determining the characteristics of the origin of basalts in the region (Pearce, 1983); c) Diagram of Rb/Ba versus Ti/Y (upper mantle range (MORB and asthenosphere), lower crust (LC), and lamproite ranges were considered a magma with low partial melting and in equilibrium with the garnet-bearing mangle

In the most recent study by Zelenski et al., (2020), which examined the concentrations of main gas species (H2O/CO2/S/HCl ratios) and isotopic data on the composition of volcanic gases in the Damavand volcano, they suggested that its origin is a hot spot/rift. According to Ritz et al., (2006), this change began 1 to 5 million years ago and coincided with the period of Damavand volcanic activity (1.8 million to 7,300 years ago) (Davidson et al., 2004).

The NW-SE trend of lava flows in the east of Damavand is significant, although no single fissure for the outflow of basic products has been identified in this area. Research has shown that these lavas probably erupted from a linear fissure caused by the activity of a fault with a NW-SE trend in the rural areas of Nova, Gilas, Ira, and Niuk. Additionally, the basaltic lavas in Pleur differ from those of other groups to the east of Damavand in terms of coordinates and sequence of eruption. Geochemical studies indicate that these two basic groups and the andesitic group originated from two separate reservoirs at different depths (Pandamoz, 1998; Hassanzadeh et al., 2001; Davidson et al., 2004; Omidian, 2007).

In general, based on various research performed on the Damavand volcano, different tectonic positions have been proposed for the magmatism of Damavand and the surrounding areas:
1. Intracontinental alkaline magmatism in the last stages of orogeny (Emami & Irannejadi, 1993)
2. Subduction of the oceanic crust of Neotethys under the continental crust of Iran (Brousse & Moine Vaziri, 1982; Emami & Irannejad, 1993; Aftabi & Atapour, 2002).

Mehdizadeh et al., (2002) and Liotard et al., (2008) attributed the increase in K_2O of volcanic rocks from the Urmia-Dokhtar magmatic belt to the Damavand volcano to an increase in the depth of the Benioff zone. The subduction age is related to the beginning of subduction of the Caspian sub-oceanic crust in the Late Neogene (Priestley, 1994) or earlier, to the formation of the Zagros Belt (Aftabi & Atapour, 2002). Although geophysical evidence does not confirm the presence of a subducted plate below Damavand and Central Alborz, the geochemical properties of Damavand magmatism related to the post-collision tectonic environment of Alborz are similar to the geochemical properties of the Tibetan post-collision environments (Gao et al., 2005), for which the presence of an old sheet is suggested (Lotard et al., 2008).
3. In-plane hotspot (within-plate) (Davidson et al., 2004)
4. Mantle uplift and lithospheric delamination (Jung et al., 1976; Mirnejad et al., 2010)

Eskandari, (2016) proposed a geodynamic model for the origin of Damavand magmatism, emphasizing the roles of the lower crust, lithosphere, and asthenosphere mantle, with varying ratios and percentages of influence on the formation of primary magma. The change in the tectonic regime of the central Alborz region, which has shifted from compressional to tensile since approximately 5 million years ago, has created a suitable environment for the ascent and emplacement of magma along the bends of faults and fractures (Ritz et al., 2006). Hassanzadeh et al., (2006) and Ritz et al., (2006) mentioned this change in kinematics approximately 1.5 million years ago, coinciding with the onset of Damavand volcanic activity. In the most recent research, which combines geophysical results with tectonic results (Shabanian et al., 2012), the Damavand volcano is located at the intersection and transition between two regimes: 1) a compressional tectonic regime effective in the western part and a tensile tectonic regime effective in the eastern part. According to these authors, these regimes have played a role in creating suitable conduits in the crust for the passage, storage, and eruption of magma. Therefore, the studied rocks were formed in a tensile environment (intracontinental rift) and due to the action of the strike-slip faults (Ira and Nava or their sub-branches) (Eskoi & Omidian, 2013).

Considering the tectonic conditions in Central Alborz, the compressional regime has prevailed for a long time. Therefore, there must be a long time between magma production and its ascent and eruption. Based on geophysical, mineralogical, and geochemical data from Damavand and its surrounding areas, Eskandari et al., (2018) believe that basaltic magma was produced at the lithosphere-asthenosphere boundary. Subsequently, the magma ascends to the

upper parts and is deposited in the lower crust due to the density difference between the mantle and the lower crust. Based on clinopyroxene pressure geometry and phase equilibria, the approximate depth of this magma storage area ranges from 28 to 10 km, which is equivalent to a pressure of 8 to 35 kbar. Instead of a single magma reservoir, there may be several smaller storage areas between 10 and 6 kbar.
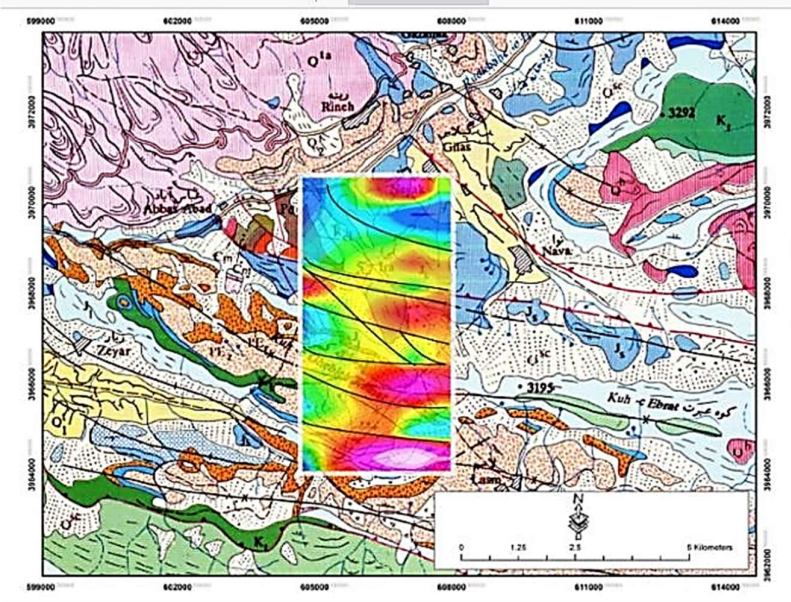

Figure 12. Nova, Ira faults, and other faults detected by magnetometric studies by (Eskoi & Omidian, 2013)
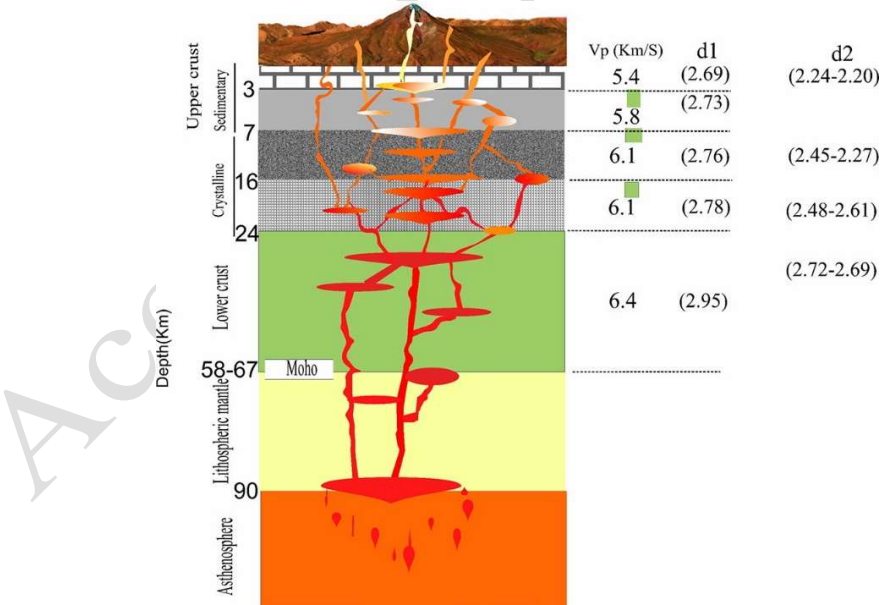
Figure 13. Schematic illustration of the magma plumbing system of the Damavand volcano. The depth of Moho is based on geophysical models (Sodudi et al., 2009; Abbasi et al., 2010). The Vp and crustal structures and densities are from Abbasi et al., (2010). The two upper green rectangles indicate the depth of hot bodies (probable magma chambers) based on seismic tomography (Mostafanejad et al., 2011; Shomali & Shirzad, 2014). The lower green rectangle shows the position of the solidified magma chamber (Mostafanejad et al., 2011). The d1 is the density of crustal rocks, and d2 is the density of magma calculated through the MELTS Eskandari et al., (2018)
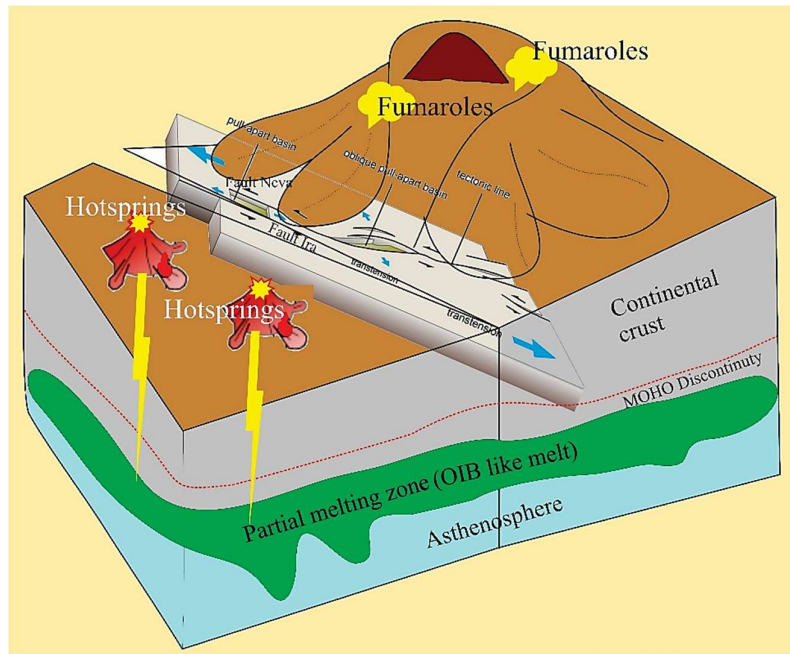
Figure 14. Schematic diagram of the Pull-apart basins regarding the formation of rocks in the study area and the Damavand

Given the presence of hot springs, recorded surface thermal anomalies, vent activities, and fault trends around Damavand, it can be inferred that the rocks of the region were formed by the melting of a metasomatized mantle in an extensional environment characterized by divergent basins or pull-apart basins (Fig. 14). Examples include the geothermal fields and volcanic activities of the Salton Sea and Cerro Prieto at the northwestern end of the Gulf of California. According to the classification by Mann et al., (1983), most rift basins are elongated, with sizes varying from less than 30 km² to 500 km², and an average regional area of 140 km². The depth of these basins varies from 800 m to more than 2000 m (Sutrisno et al., 2019). The origin of the volcanic rocks in the study area and around Damavand is a hot spot/rift in a rifting basin, which, after the eruption, still contains a hot and probably molten mass at depths of 4 to 7 km. This statement is confirmed by the chimneys, fumarolic activities, and hot springs in the area, as well as the thermal anomalies. It is worth noting that no thermal manifestation appears in the middle of the basin without any associated faults. All these features are located either on the slopes of adjacent volcanic centers or along the main strike-slip faults or normal faults that characterize the basin (Fig. 14).

Conclusions

Volcanic rocks, ranging from alkali-olivine basalt to trachyandesite, can be seen along Haraz Road. Damavand volcanic lavas contain minerals with sieve textures and oscillatory zoning, demonstrating the influence of complex processes in multiple magmatic reservoirs and an open system. Contrary to the simple fractionation process, LREEs and some LILEs are reduced from alkaline basalts to trachyandesites. Multi-element diagrams also show the depletion of these elements and P in trachyandesites compared to the basalts. Generally, REE patterns in multi-element diagrams do not fully confirm a tectonic environment and have the characteristics of both subduction and OIB environments. A comparison of some indicators of crustal contamination, such as elemental ratios, shows that trachyandesites have more crustal contamination than alkaline olivine basalts. Meanwhile, high ratios of Ce/Pb, Nb/U, Ba/Nb, and Th/La, and low ratios of Sm/La, in alkaline olivine basalts with low silica percentages and

high magnesium, indicate that these lavas are more affected by source contamination with crustal materials.

Conflict of Interest

The authors declare that they have no conflict of interest with respect to the author or publication of this article.

References

Abbassi, A., Nasrabadi, A., Tatar, M., Yaminifard, F., Abbassi, M., Hatzfeld, D., Priestley, K., 2010. Crustal velocity structure in the southern edge of the Central Alborz (Iran). Journal of Geodynamics, 49(2): 68-78.

Aftabi, A., Atapour. H., 2002. Regional aspects of shoshonitic volcanism in Iran. Episodes, 23: 119-125.

Aldanmaz, E., Pearce, J.A., Thirlwall, M., Mitchell, J., 2000. Petrogenetic evolution of late Cenozoic, post-collision

Volcanism in western Anatolia, Turkey. Journal of Volcanology and Geothermal Research, 102(1-2): 67-95.

Allen, M.B., Ghassemi, M.R., Shahrabi, M., Qorashi, M., 2003. Accommodation of the late Cenozoic oblique shortening in the Alborz range, northern Iran. Journal of Structural Geology, 25: 659-672.

Allenbach, P.,1966. Geologie und Petrographie des Damavand und seiner Umgebung (Zentral-Elbruz, Iran). Mitteilungen aus dem Geologischen Institut der Eidg. Technischen Hochschule und der Universität Zürich, 63, pp 114.

Agard, P., Omrani, J., Jolivet, L., Mouthereau, F., 2005. Convergence history across Zagros (Iran): deposit, Northwest Iran. Journal of Economic Geology, 101: 1455-1496.

Assereto, R., 1966- The Jurassic Shemshak Formation in Central Alborz (Iran). Rivista Italiana di Paleontologia E stratigrafia, 72: 1133-1182.

Asudeh, I., 1982. Seismic structure of Iran from surface and body wave data. Geophysical Journal International, 71(3): 715-730.

Berberian, M., 1976. An explanatory note on the first seismotectonic map of Iran, a seismotectonic review of the country. Contribution to the seismotectonics of Iran (Part III).

Brousse, R., Moine Vaziri, H.,1982. L'association shoshonitique du Damovand (Iran) Sonferdruck aus der Geologischen Rundschau, 71: 687-699.

Coban, H.,2007. Basalt magma genesis and fractionation in collision- and extension-related provinces, A comparison between eastern, central, and western Anatolia. Earth Science Reviews, 80:219-238.

Carter, L.B., Dasgupta, R.,2015. Hydrous basalt-limestone interaction at crustal conditions: implications for generation of ultracalcic melts and outflux of CO_2 at volcanic arcs. Earth and Planetary Science Letters, 427: 202-214.

Carter, L.B., Dasgupta, R., 2016. Effect of melt composition on crustal carbonate assimilation: implications for the transition from calcite consumption to skarnification and associated CO_2 degassing. Geochemistry, Geophysics, Geosystems, 17: 3893-3916.

Darvishzadeh, A., 2004. Geology of Iran, Amirkabir Publishing, 343 p.

Davidson, J.P., Morgan, D.J., Charlier, B.L.A., Harlou, R., Hora, J.M., 2007. Microsampling and Isotopic Analysis of Igneous Rocks: Implications for the Study of Magmatic Systems. Annual Review of Earth and Planetary Sciences, 35: 273-311.

Dehghani, G., Makris, J., 1984. The Gravity Field and Crustal Structure of Iran. Neues Jahrbuch für Geologie und Paläontologie Abhandlungen, 168: 215-229.

Emami, M.H., Irannejadi, M.R., 1993. Petrology and volcanology study of Damavand volcano. Journal of Earth Sciences, 2: 232, 86.

Eichelberger, C. J., 1978. Andesitic volcanism and crustal evolution. Nature, 275: 21-27.

Elliott, T., 2003. in Inside the Subduction Factory, J. M. Eiler, Ed. Geophysical Monograph Series, AGU, 138: 23-45.

Eskandari, A., 2016. Investigation of magmatic evolution of lava in Damavand volcano based on

mineralogical and geochemical properties, PhD Thesis, Kharazmi University. 313p.

Eskandari, A., Amini, S., DeRosa, R., Donato. P., 2018. Nature of the magma storage system beneath the Damavand volcano (N. Iran): An integrated study. Lithos, 300-301;154-176.

Freda, C., Gaeta, M., Misiti, V., Mollo, S., Dolfi, D., Scarlato, P., 2008. Magma-carbonate interaction: an experimental study on ultrapotassic rocks from Alban Hills (Central Italy). Lithos, 101: 397-415.

Frisch, W., Meschede, M., Blakey, R.C.,2011. Plate Tectonics: Continental Drift and Mountain Building. Springer: Berlin, Germany. 212p.

Gao, S., Rudnick, R.L., Yuan., H.L., Liu, X.M., Liu Y.S., Xu., W.L., Ling, W.L., Ayers, J., Wang, X.C., Wang, Q.H., 2004. Recycling lower continental crust in the North China craton. Nature, 43: 892-897.

Hassanzadeh, J., Pandamoz, A., Davidson, J., Stockley, D., Bashkooh, B., 2001. Geology of Iran, 49-44.

Hastie, A.R., Kerr, A.C., Pearce, J.A., Mitchell, S.F., 2007. Classification of altered volcanic island arc rocks using immobile trace elements: development of the Th-Co discrimination diagram. Journal of Petrology, 48:2341-2357.

Hawkesworth, C. J., Gallager, K., Hergt, J.M., McDoermott, F., 1994. Destructive plate margin magmatism: Geochemistry and generation. Lithos, 33: 169 - 188.

Hoang, N., Flower, M., 1998. Petrogenesis of Cenozoic basalts from Vietnam: implications for origins of a 'diffuse igneous province. Journal of Petrology, 39(3): 369-395.

Hibbard, M.J., 1981. The magma mixing origin of mantled feldspars. Contributions to Mineralogy and Petrology, 76: 158-170.

Humphreys, M.C.S., Blundy, J.D., Sparks, S.J., 2006. Magma evolution and open system processes at Shiveluch volcano: insights from phenocryst zoning. Journal of Petrology, 12: 303-334.

Iacono Marziano, G., Gaillard, F., Pichavant, M., 2007. Limestone assimilation and the origin of CO_2 emissions at the Alban Hills (Central Italy): constraints from experimental petrology. Journal of Volcanology and Geothermal Research, 166: 91-105.

Iacono-Marziano, G., Gaillard, F., Pichavant, M., 2008. Limestone assimilation by basaltic magmas: an experimental re-assessment and application to Italian volcanoes. Contributions to Mineralogy and Petrology, 155: 719-738.

Irvin, T., Baragar, W.R.A., 1971. A guide to the Chemical classification of the common volcanic rocks. Canadian Journal of Earth Science Letters, 8: 523-548.

Jung, D., Kuersten, M.O.C., Tarkian, M., 1976. Post-Mesozoic volcanism in Iran and its relation to the subduction of the Afro-Arabian under the Eurasian Plate, In: Pilger, A., Roesler, A. (Eds.), Afar between Continental and Oceanic Rifting, 2:175-181.

Kress, V.C., Ghiorso, M.S., 2004. Thermodynamic modeling of post-entrapment crystallization in igneous phases. Journal of Volcanology and Geothermal Research, 137(4): 247-260.

Kuo, H., 1950. Petrology of the Hakone Volcano and the Adjacent Areas, Japan. Bulletin of the Geological Society of America, 61: 957-1020.

Le Bas, M. J., Le Maitre, R.W., Streckeisen, A., Zanettin, B., 1986. A chemical classification of volcanic rocks based on the total alkali-silica diagram. Journal of Petrology, 27: 745-750.

Liotard, j.M., Dautria, j.M., Bisch, D., Condmines, j., Mehdizade, H., Ritz, F., 2008. Origin of the absarokite-banakite association of the Damavand volcano (Iran): trace elements and Sr, Nd, Pb isotope constraints. International Journal of Earth Sciences, 97:89-102.

Lustrino, M.,2005. How the delamination and detachment of the lower crust can influence basaltic magmatism. Earth-Science Reviews, 72(1):21-38.

Mann, P., Hempton, M.R., Bradley, D.C., Burke, K., 1983. Development of pull-apart basins. The Journal of Geology, 91: 529-554.

Mckenzie, D.P., Onions, R.K., 1991. Partial melt distributions from inversion of rare earth element concentrations. Journal of Petrology, 1:1021-1091.

Mehdizadeh, H., Liotard, J.M., Dautria, J.M., 2002. Geochemical characteristics of an intracontinental shoshonitic association: the example of the Damavand volcano, Iran. Comptes Rendus Geoscience, 334:111-117.

Mirnejad, H., Hassanzadeh, J., Cousens, B.L., Taylor, B.E., 2010. Geochemical evidence for deep mantle melting and lithospheric delamination as the origin of the inland Damavand volcanic rocks of northern Iran, Journal of Volcanology and Geothermal Research, 198:288-296.

Moin Vaziri, H., 1998. Introduction to Magmatism in Iran, Tarbiat Moallem University Press, 445 p.

Mostafa Nejad, A., Shomali, Z.H., Mottaghi, A.A., 2011. 3-D velocity structure of Damavand volcano, Iran, from local earthquake tomography. Journal of Asian Earth Sciences, 42:1091-1096.

Nelson, S.T., Montana, A., 1992. Sieve-textured plagioclase in volcanic rocks produced by rapid decompression. American Mineralogist, 77:1249-1242.

Philpotts, A. R., 1990. Principles of Igneous and Metamorphic Petrology, Prentice Hall, NJ; 498 p.

Omidian, P., 2007. Determining the tectonic position of the Damavand volcano based on structural and geochemical evidence, BS thesis, Master of Petrology, Department of Geology, Faculty of Science, University of Tehran.

Omrani, J., Agard, P., Whitechurch, H., Benoit, M., Prouteau, G., Jolivet, L., 2008. Arc magmatism and subduction history beneath the Zagros Mountains, Iran: a new report of adakites and geodynamic consequences. Lithos,106(3): 380-398.

Oskooi, B., Rouhani, M.J., Omidian, P., Abedi, M., 2018. Analysis of magnetic data on basalts of the Pleur region. Journal of Applied Geophysical Research, 4(2): 323-337.

Pand Amooz, A., 1998. Determining the position of basaltic flows in the sequence of the Damavand volcano, Master's Thesis, University of Tehran.

Pearce, J. A., 1982. Trace element characteristics of lavas from destructive plate boundaries, John Wiley and Sons, U.K., 525-548.

Perugini, D., Poli, G., 2012. The Mixing of Magmas in Plutonic and Volcanic Environments: Analogies and Differences. Lithos, 153: 261-277.

Pichavant, M., Scaillet, B., Pommier, A., Iacono-Marziano, G., Cioni, R., 2014. Nature and evolution of primitive Vesuvius magmas: an experimental study. Journal of Petrology, 55: 2281-2310.

Prelević, D., Jacob, D.E., Foley, S.F., 2013. Recycling plus: a new recipe for the formation of Alpine-Himalayan orogenic mantle lithosphere. Earth and Planetary Science Letters, 362:187-197.

Priestley, K., Baker, C., Jackson, J., 1994. Implications of earthquake focal mechanism data for the active tectonics of the South Caspian Basin and surrounding regions. Geophys,118:111-141.

Renjith, M. L., 2014. Geoscience Frontiers Micro-textures in plagioclase from 1994 to 1995 eruptions, Barren Island Volcano: Evidence of dynamic magma plumbing system in the Andaman subduction zone. Geoscience Frontiers, 5(1): 113-126.

Richards, J., Wilkinson, D., Ullrich, T., 2006. Geology of the Sari Gunay epithermal gold. Economic Geology, 101 (8):1455-1496.

Ritz, J.F., Nazari, H., Ghassemi, A., Salamati, R., Shafei, A., Solaymani, S., Vernant, P., 2006. Active transtension inside Central Alborz: a new insight into northern Iran-southern Caspian geodynamics. Geology, 34: 477-480.

Schandl, E.S., Gorton, M.P., 2002. Application of high field strength elements to discriminate tectonic settings in VMS environments. Economic Geology, 97: 629-642.

Sigurdsson, H., 1971. Feldspar relations in a composite magma. Lithos, 4: 231-238.

Singer, B., Dungan, M.A., Layne, G.D., 1995. Textures and Sr, Ba, Mg, Fe, K, and Ti compositional profiles in volcanic plagioclase: clues to the dynamics of calc-alkaline magma chambers. American Mineralogist, 80: 776-798.

Sodoudi, F., Yuan, X., Kind, R., Heit, B., Sadidkhouy, A., 2009. Evidence for a missing crustal root and a thin lithosphere beneath the Central Alborz by receiver function studies. International Journal of Geophysics, 177 (2): 733-742.

Shomali, Z.H., Shirzad, T., 2014. Crustal structure of Damavand volcano, Iran, from ambient noise and earthquake tomography. Journal of Seismology, 19: 191-200.

Stöcklin, J., 1974. Northern iran: Alborz mountains. Geological Society, London, Special Publications, 4(1):213-234.

Stöcklin, J., Nabavi, M.H., 1973. Tectonic Map of Iran 1:2500000 Geological Survey of Iran,

Stöcklin, J., Ruttner, A., Nabavi, M., 1964. New data on the lower Paleozoic and Precambrian of North Iran. Geological Survey of Iran, Reports, 1: 29.

Sutrisno, L., Bonte, D., Daud, Y., Smit, J., Beekman, F., Van Wees, J.D., Purwanto, W., 2019. Assessing the role of pull-apart basins for high-temperature geothermal resources in transcurrent tectonic settings: Sumatra and California compared. European Geothermal Congress, 11-14.

Tchameni, R., Pouclet, A., Penay, J., Ganwa, A. A., Toteu, S.F., 2006. Petrography and geochemistry of the Ngaondere Pan - African granitoids in Central North Cameroon: Implications for their sources

and geological setting. Journal of African Earth Sciences, 44: 511 -529.

Taylor, S.R., McLennan, S.M., 1985. The continental crust: its composition and evolution.

Turner, S., Arnaud, N., Liu, J., Rogers, N., Hawkesworth, C., Harris, N., Vanclasteren, P., Deng, W., 1996. Post-collision, Shoshonitic Volcanism on the Tibetan Plateau: Implications for convective thinning of lithosphere and the Source of ocean island basalt. Journal of Petrology, 37(1):45-71.

Wilson, M., 1989. Igneous petrogenesis a global tectonic approach. Unwin Hyman, London, 466 pp.

Verma, S. P., Guevara, M., Agrawal, S., 2006. Discriminating four tectonic settings: Five new geochemical diagrams for basic and ultrabasic volcanic rocks based on log—ratio transformation of major-element data. Journal of Earth System Science, 115(5):485-528.

Vernant, P., Nilforoushan, F., Chery, J., Bayer, R., Djamour, Y., Masson, F., Tavakoli, F., 2004. Deciphering oblique shortening of central Alborz in Iran using geodetic data. Earth and planetary science letters, 223(1-2):177-185.

Viccaro, M., Barca, D., Bohrson, W. A., Oriano, C. D., Giuffrida, M., Nicotra, E., and Pitcher, B. W., 2016. Lithos Crystal residence times from trace element zoning in plagioclase reveal changes in magma transfer dynamics at Mt. Etna during the last 400 years. Lithos, 248-251: 309-323.

Viccaro, M., Giacomoni, P. P., Ferlito, C., and Cristofolini, R., 2010. Dynamics of magma supply at Mt. Etna volcano (Southern Italy) as revealed by textural and compositional features of plagioclase phenocrysts. Lithos, 116(1-2): 77-91.

Ustunisik, G., Kilinc, A., Nielsen, R.L., 2014. New insights into the processes controlling compositional zoning in plagioclase, Lithos, 200-201: 80-93.

Zadsaleh, M., Masoudi, F., Pourkhorsandi, H., Fontijn, K., 2022. Application of plagioclase mineral textures in lava, ash fall, and surge deposits to examine young Damavand magmatic processes. Scientific Quarterly Journal, Geosciences, 32(124): 13-30.

Zelenski, M., Chaplygin, I., Farhadian Babadi, M., Taran, Y., Campion, R., Mehrabi, B., and Kuznetsova, O., 2020. Volcanic gas emissions from Taftan and Damavand, the Iranian volcanoes. Journal of Volcanology and Geothermal Research, 397: 106880.